Ruiz-Rus, J., Bolaños-Jiménez, R., Gutiérrez-Montes, C., Sevilla, A. & Martínez-Bazán, C. (2017, marzo). Controlled formation of bubbles in a planar co-flow configuration. International Journal of Multiphase Flow, 89, 69-80.

DOI: 10.1016/j.ijmultiphaseflow.2016.10.008

Controlled formation of bubbles in a planar co-flow configuration

J. Ruiz-Rus,[1,*] R. Bolaños-Jiménez,[1] C. Gutiérrez-Montes,[1] A. Sevilla,[2] and C. Martínez-Bazán[1]

[1] *Área de Mecánica de Fluidos, Departamento de Ingeniería Mecánica y Minera. Universidad de Jaén. Campus de las Lagunillas, 23071, Jaén, Spain.*

[2] *Área de Mecánica de Fluidos, Departamento de Ingeniería Térmica y de Fluidos. Universidad Carlos III de Madrid, 28911, Leganés, Spain.*

We present a new method that allows to control the bubble size and formation frequency in a planar air-water co-flow configuration by modulating the water velocity at the nozzle exit. The forcing process has been experimentally characterized determining the amplitude of the water velocity fluctuations from measurements of the pressure variations in the water stream. The effect of the forcing on the bubbling process has been described by analyzing the pressure signals in the air stream in combination with visualization performed with a high-speed camera. We show that, when the forcing amplitude is sufficiently large, the bubbles can be generated at a rate different from the natural bubbling frequency, f_n, which depends on the water-to-air velocity ratio, $\Lambda = u_n/u_a$, and the Weber number, $We = \rho_w u_n^2 H_o/\sigma$, where H_o is the half-thickness of the air stream at the exit slit, ρ_w the water density and σ the surface tension coefficient. Consequently, when the forcing is effective, monodisperse bubbles, of sizes smaller than those generated without stimulation, are produced at the prescribed frequency, $f_f > f_n$. The effect of the forcing process on the bubble size is also characterized by measuring the resulting intact length, l_i, i.e. the length of the air stem that remains attached to the injector when a bubble is released. In addition, the physics behind the forcing procedure is explained as a purely kinematic mechanism that is added to the effect of the pressure evolution inside the air stream that would take place in the unforced case. Finally, the position of the maximum perturbation amplitude has been determined by a one-dimensional model, exhibiting a good agreement both with experiments and numerical simulations performed with OpenFOAM.

I. INTRODUCTION

Bubble generation represents an important operation in the context of material, mineral, chemical and food industries, to name a few. Many emerging technologies, such as those related to biomedicine, require the use of monodisperse microbubbles [28]. Water aeration is another important application, characterized by the requirement of very large air throughputs (for a recent review, see [2]). The efficiency of these systems is controlled by the amount of gas dissolved in the liquid per unit of time, and the dissolution rate is proportional to the surface of the gas-liquid interface. A possible way to increase the interfacial area is to decrease the volume of the injected bubbles, what can in principle be achieved using porous plates or microfluidic devices. However, these systems are prone to clogging issues due to the smallness of the injection ports. Thus, developing robust devices able to inject very large air flow rates with small bubbles is still a challenging engineering problem. The configuration studied in the present work represents a promising route to increase the efficiency of industrial-scale water aeration operations.

Many techniques have been developed in the last decades to massively generate small monodiperse bubbles. One of the most extended methods is the co-flow configuration, in which the gas flow discharges inside a laminar liquid stream that flows in the same direction. The cylindrical co-flow geometry has been extensively studied [7, 10, 12, 26, 30, 31] and is widely used nowadays, playing a relevant role in microfluidics [11, 34]. The formation of bubbles in a planar co-flow configuration has also been studied [4, 5, 14, 15]. The results of these works, devoted to the experimental, theoretical and numerical study of the bubble formation process, reveal that the periodic bubbling regime that is naturally established in the planar case produces bubbles of much larger volume than in the cylindrical geometry. Indeed, in the planar case the quasi-two-dimensional dynamics of the flow provides bubbles of pancake-like shape whose spanwise length is determined by the corresponding dimension of the air nozzle. Therefore, finding ways to decrease the size of the bubbles and increase their formation frequency is crucial for the practical application of the planar co-flow device.

Several forcing methods have been investigated in the past to control the formation of bubbles by actuating on the gas stream. For instance, the use of pulsed acoustic pressure waves in the gas phase [1, 22, 32] or the direct actuation over the feeding gas stream [27]. The use of mechanical vibrations of the injector has also been explored [35]. In contrast, only a few studies can be found on the forcing of the liquid phase, mainly in the field of bubble columns to improve

* jrrus@ujaen.es

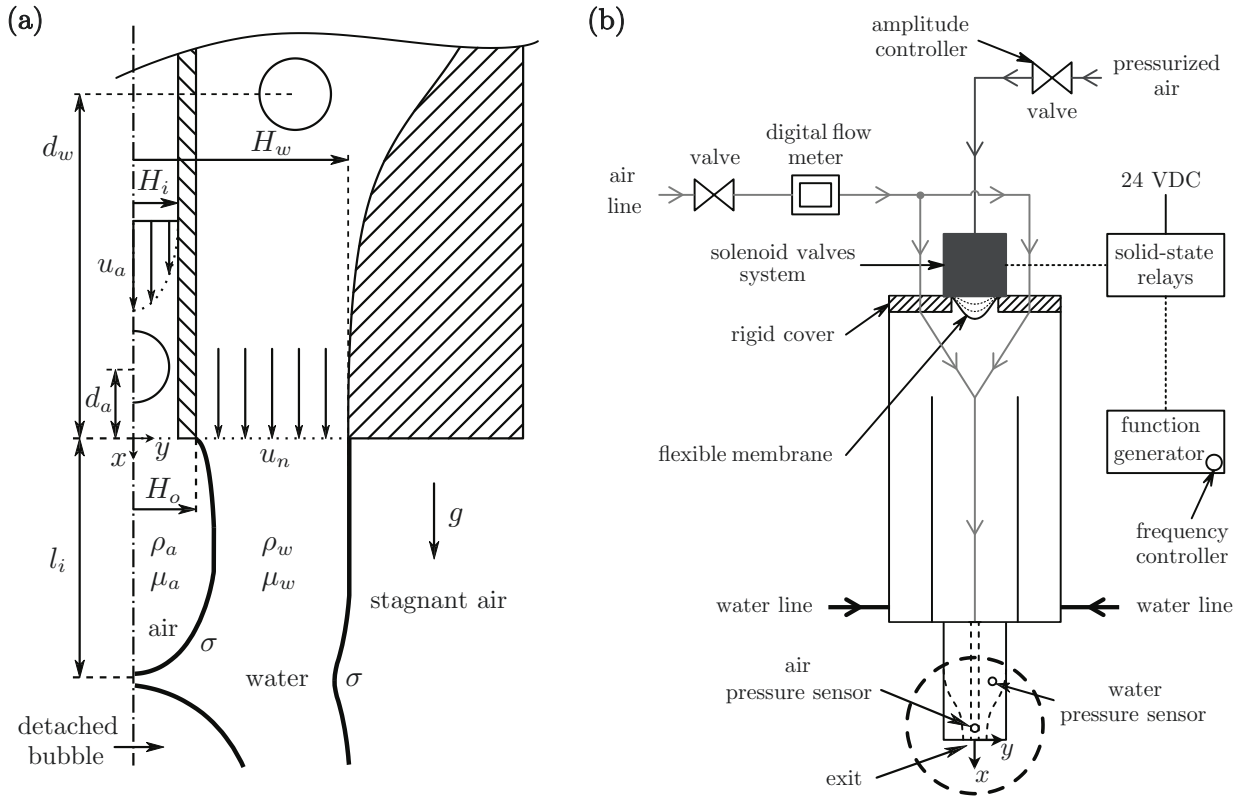

FIG. 1. (a) Sketch of the air-water co-flowing streams at the exit of the nozzle in the side plane (x, y), showing the natural bubble formation and indicating the main geometrical characteristics, the dimensional parameters of the unforced problem, and the position of both the air and water gauge pressure sensors. (b) General sketch of the experimental facility, including the forcing device. The region highlighted with a dashed circle corresponds to the exit of the nozzle, sketched in Fig. 1(a).

their performance by low-frequency pulsations of the liquid [18], and in microbubble generation by applying an external ultrasonic field to the liquid phase [21].

The method proposed in the present work consists of forcing the liquid flow rate by harmonic stimulation. Although, to the best of our knowledge, this technique has not been explored before to control the bubble formation process in co-flow devices, it is a widespread technique to control the break-up of cylindrical liquid jets [6, 9, 13, 25] and sheets [20, 24, 33]. Therefore, we have developed a system to control the generation of bubbles in a planar water-air-water sheet by harmonically modulating the flow rate of the water stream, although it could easily be implemented in other types of configurations.

The manuscript is organized as follows. Section II is devoted to the description of both the experimental and numerical work: the experimental facility and techniques are detailed in Subsection II A, while the numerical method and procedure are described in Subsection II B. Next, in Section III, the experimental results are presented, where the effectiveness of the forcing is first characterized in Subsection III A, followed by Subsection III B, where the conditions for effective stimulation are characterized through the critical forcing amplitude and the length of the intact air ligament that remains attached to the injector once a bubble is formed. Next, in Section IV, the forcing effect is described by means of a theoretical one-dimensional model. Finally, Section V is devoted to conclusions.

II. EXPERIMENTAL AND NUMERICAL METHODS

A. Experimental set-up

The experimental facility described by Bolaños-Jiménez et al [4] and Gutiérrez-Montes et al [14] has been used in the present work to create a planar air sheet of outer half thickness $H_o = 0.455$ mm surrounded by a pair of symmetrical parallel water streams that discharge into a stagnant air atmosphere, with a thickness $h_0 = H_w - H_o = 1.945$ mm, being $H_w = 2.4$ mm the distance from the outer interface to the central plane (Fig. 1a). The set-up basically consists of

two parallel thin walls placed at a distance $2\,H_i \simeq 0.47$ mm that confine the air stream, and two exterior nozzle-shaped walls for the co-flowing water streams separated by a distance $2\,H_w$ at the outlet. The spanwise length of the injector, perpendicular to the plane sketched in Fig. 1(a), is $b = 41.75$ mm, two orders of magnitude larger than the air sheet thickness, providing a quasi-two-dimensional configuration. For the purposes of the present work, the facility was modified to incorporate a forcing system, sketched in Fig. 1(b). The design of the inner channel of the whole nozzle assures that, at the exit of the injector, the velocity profile is fully developed in the air stream and nearly uniform in the water one (Fig. 1a). The pressure drop along the air channel was always much larger than the pressure fluctuations inside the forming bubble, ensuring thus a constant air flow supply [12]. The water was supplied to both outer nozzles from a feeding vessel placed above them, minimizing the transverse velocity components. Both the feeding air and water flow rates, Q_a and Q_n, were controlled through precision valves and measured with digital mass flow meters. The average velocities at the nozzle exit, calculated by dividing the flow rate by the corresponding cross section, were varied from $u_a \simeq 13$ m/s to $u_a \simeq 19$ m/s and $u_n \simeq 1.5$ m/s to $u_n \simeq 2.5$ m/s, for the air and the water streams respectively. The remaining parameters involved in the unforced problem (Fig. 1a) are the air-water surface tension coefficient, σ, the water and air viscosities, μ_w and μ_a, the water and air densities, ρ_w and ρ_a, and the gravitational acceleration, g. Viscous effects can be neglected in both the water and air flows downstream of the nozzle outlet, since the corresponding Reynolds number ranges are $3000 \lesssim Re_w = \rho_w u_n h_0/\mu_w \lesssim 5000$, and $300 \lesssim Re_a = \rho_a u_a H_o/\mu_a \lesssim 500$ [4, 14]. In addition, the gas-to-liquid density ratio was constant in all experiments, $S = \rho_a/\rho_w \simeq 0.0012$. Finally, the Froude number based on the length of the intact ligament, l_i, which is the lump of air that remains attached to the nozzle exit after the pinch-off of a bubble (see Fig. 1a), is $Fr = u_n^2/(g l_i) \gg 1$, so that the effect of gravity can be neglected. Therefore, there are only two dimensionless parameters governing the unforced bubbling configuration, namely the Weber number, $We = \rho_w u_n^2 H_o/\sigma$, and the water-to-air velocity ratio, $\Lambda = u_n/u_a$, that were varied in this work within the ranges $14 \lesssim We \lesssim 40$ and $0.08 \lesssim \Lambda \lesssim 0.16$. The bubbling regime can be experimentally induced by properly setting the values of We and Λ, as described by Bolaños-Jiménez et al [4]. According to the range of values of We and Λ considered in the present work, the obtained natural bubble formation frequencies varied from $f_n \simeq 100$ Hz to $f_n \simeq 200$ Hz.

To register the pressure variations inside the air and water streams, two gauge pressure sensors were placed at distances $d_a = 3$ mm and $d_w = 65$ mm upstream from the nozzle exit (Fig. 1a). The temporal evolution of the gauge pressure registered inside the air channel, $p_a(t)$, provides a convenient description of a bubble formation event [14], while the water gauge pressure, $p(t)$, allows to characterize the forcing process of the water flow. The forcing device is placed on top of the feeding water vessel (Fig. 1b), and its performance is based on the deformation of a flexible silicone membrane that induces a variation of the water flow rate. To induce an oscillatory deformation of the membrane, its upper side is pushed and pulled through the alternative injection and suction of pressurized air, controlled by a system of high-speed pneumatic solenoid valves (MATRIX model number 821NC2/2). These valves are driven by electric on/off signals (24-0 VDC) from solid-state relays which are excited by a square signal from a tunable-frequency function generator (YOKOGAWA model number FG110), that allows to select the forcing frequency, f_f. The forcing amplitude is set by a precision valve that controls the pressurized air flow rate feeding the stimulation system (Fig. 1b).

The forcing device induces a modulation of the water flow rate. Thus, to characterize the velocity modulation at the exit of the injector it is necessary to translate the pressure signals, recorded by the pressure sensor, into velocity. The liquid volume conservation equation requires the deformations of the membrane to instantaneously induce a variation of the water flow rate at the exit of the nozzle, $Q(t)$, that differs from its unforced value, Q_n. Hence, the disturbance results in a modulation of the water flow rate at the exit,

$$Q(t) = Q_n + Q'(t), \tag{1}$$

where $Q'(t) \ll Q_n$ represents the flow rate disturbance, which can be obtained from the signal registered by the water pressure sensor, $p(d_w, t) = p_n(d_w) + p'(d_w, t)$. Here, p_n represents the unforced gauge pressure and $p'(d_w, t)$ the pressure disturbance, which can be approximated by a harmonic signal, as shown in Figs. 2(a, c)

$$p'(d_w, t) = \zeta \cos(\omega t + \varphi), \tag{2}$$

where ζ is the amplitude of the water pressure disturbance, $\omega = 2\pi f_f$ the angular frequency, and φ the phase with respect to the pinch-off event associated with the formation of the previous bubble. It can be seen in Fig. 2(a) that the experimental water pressure signal can be well described by Eq. (2). Moreover, since $Re_w \gg 1$, the inviscid momentum equation for the water in the streamwise direction inside the nozzle can be expressed as

$$\frac{\partial u_w}{\partial t} + u_w \frac{\partial u_w}{\partial x} = -\frac{1}{\rho_w}\frac{\partial p}{\partial x} + g, \tag{3}$$

being u_w the streamwise component of the water velocity. According to Eq. (1), if Eq. (3) is linearized and taking into account that the lowest value of $f_f\,L$ in the experiments performed here was much larger than u_n, being $(f_f\,L)_{min} =$

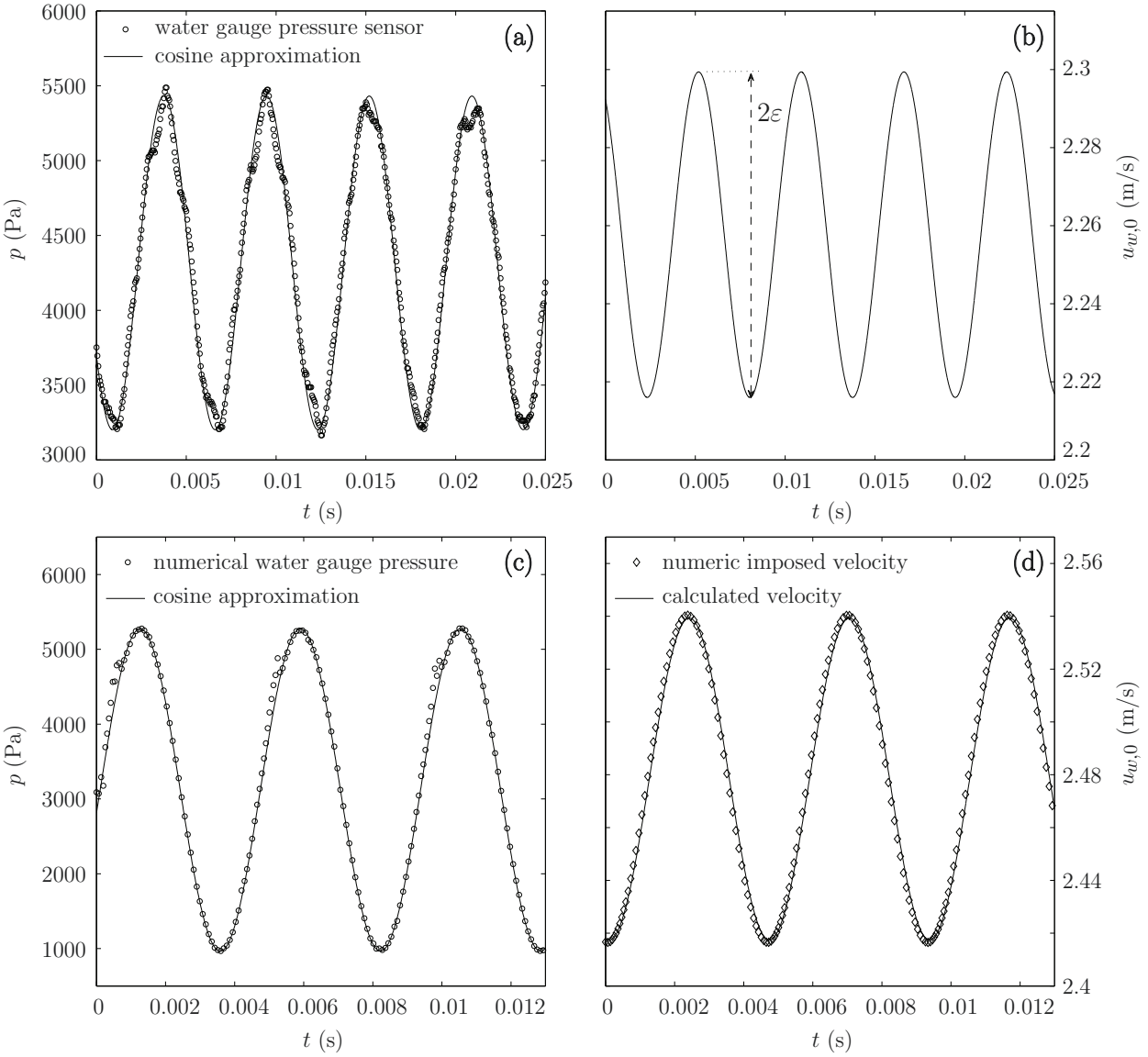

FIG. 2. Time series of water pressure and velocity extracted from the experiments (a,b, corresponding to $We = 32.2$, $\Lambda = 0.152$, $f_f = 175$ Hz and $\epsilon = 0.018$), and the simulations (c,d, for $We = 38.8$ and $\Lambda = 0.147$, $f_f = 216$ Hz and $\epsilon = 0.025$). (a) Experimental gauge pressure together with a cosine fit. (b) Velocity at the nozzle exit obtained with Eq. (5), from which ε is obtained. (c) Numerical gauge pressure at a distance from the nozzle exit equal to d_w together with a cosine fit. (d) Comparison of the imposed velocity and the calculated one using Eq. (5).

$11.5\,u_n \gg u_n$, we obtain

$$\frac{1}{A(x)}\frac{dQ'(t)}{dt} = -\frac{1}{\rho_w}\frac{\partial p'}{\partial x}, \tag{4}$$

where $A(x)$ is the cross section of the water channel and $L = 150$ mm is the length of the water nozzle. Integrating Eq. (4) between d_w and the exit of the nozzle, $x_0(x = 0)$, where the pressure inside the water sheets is the atmospheric one [4], the modulation of the water flow rate and, thus, of the water velocity, $u'_w(t)$, can be obtained as,

$$Q'(t) = \frac{1}{\rho_w K}\int_{t_0}^{t} p'(d_w, t)dt \rightarrow u'_w(t) = Q'(t)/A(x_0), \tag{5}$$

where $K = \int_{d_w}^{x_0}[1/A(x)]dx \simeq 300$ m^{-1} is a constant which depends on the water channel geometry. Equation (5) has been integrated with the initial condition $Q'(t_0) = 0$, being t_0, according to Eq. (2), the time in which the disturbance $p'(d_w, t_0)$ reaches a local maximum. Therefore, the forcing process can be described as a modulation of the water velocity

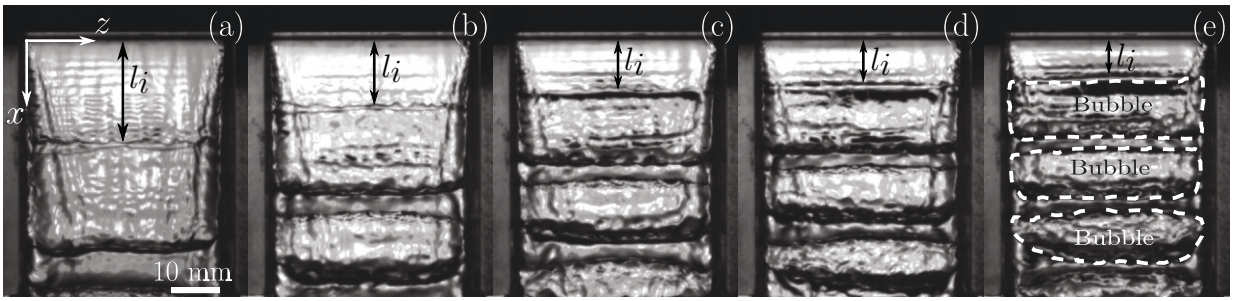

FIG. 3. Experimental images in the spanwise (x, z) plane corresponding to $u_n = 1.8$ m/s ($We = 21.6$) and $u_a = 13.9$ m/s ($\Lambda = 0.133$), (a) in the natural bubbling regime with $f_n = 118$ Hz, and (b)-(e) for different cases of effective forcing with $\epsilon = \epsilon_c$ at (b) $f_f = 150$ Hz, (c) $f_f = 175$ Hz, (d) $f_f = 200$ Hz and (e) $f_f = 225$ Hz. In each panel l_i indicates the associated intact ligament, which decreases as f_f increases. As example, the individual formed bubbles are highlighted in panel (e).

at the nozzle exit of the form $u_{w,0}(x = 0, t) = u_n + u'_w(t)$. Considering that $p'(d_w, t)$ in Eq. (5) is given by Eq. (2), the water velocity at the outlet can be expressed as,

$$u_{w,0}(t) = u_n + \varepsilon \sin(\omega t + \varphi), \tag{6}$$

where $\varepsilon = \zeta/[\rho_w \omega K A(x_0)]$ is the amplitude of the water velocity fluctuations as shown in Fig. 2(b), which depends on the amplitude and the frequency of the induced pressure disturbances, ζ and ω. Thus, the value of ε, together with the forcing frequency, $f_f = \omega/(2\pi)$, constitute the two parameters that define the stimulation of the water flow. In dimensionless terms, the forcing process can be characterized by the Strouhal number, defined as $St = f_f h_0/u_n$, and the dimensionless velocity amplitude, $\epsilon = \varepsilon/u_n$.

The experiments were conducted by firstly setting an unforced bubbling regime, identified by a given value of both u_n (or We) and u_a (or Λ), with an associated natural bubble formation frequency, f_n. After a periodic bubble generation process was achieved, a forcing frequency, $f_f > f_n$, was imposed with a function generator, and the forcing amplitude was smoothly and monotonically increased. In addition, to investigate the existence of hysteresis, the amplitude was also decreased in the same way, but no hysteresis was detected. The forcing frequency was varied from $f_f \simeq 150$ Hz to $f_f \simeq 250$ Hz, being the latter value given by the maximum air flow rate that the solenoid valve system was able to supply. Finally, the spanwise (x, z) view of the sheets was recorded using a Photron high-speed camera at frame rates between 15,000 s^{-1} and 20,000 s^{-1}, with an acquisition box of 256 × 304 pixels. A spatial resolution of around 100 μm/pixel was achieved using a Sigma 105 mm microlens and backlighting technique. The high-speed movies were synchronized with the lectures of the two gauge pressure sensors through a data logger system. Figure 3 shows several snapshots extracted from the high-speed movies, corresponding to a natural bubbling regime (Fig. 3a) and different forced cases (Fig. 3b-e) at $We = 21.6$ and $\Lambda = 0.133$. All the images correspond to the pinch-off time, at which the upper bubble detaches from the injector at a distance l_i indicated in the images. The panels show the periodic formation of nearly monodisperse, elongated bubbles in the spanwise plane (x, z), as highlighted in Fig. 3(e). It is worth noticing that the intact length, l_i, and the bubble size decrease as the forcing frequency increases, as will be described in detail later on.

B. Numerical simulations

In addition to the experiments described in subsection II A, two-dimensional, planar numerical simulations of the bubbling process were also conducted using the numerical models already documented and validated by Gutiérrez-Montes et al [14, 15]. The main purpose of these simulations was to describe the time evolution of the interface in the (x, y) plane, since this view was not available in the experiments but is crucial to investigate the physical mechanisms leading the bubble generation process. The simulations were performed with the open source code OpenFOAM (http://www.openfoam.com), through the solver *interFOAM*, which implements a Volume of Fluid (VOF) interface-capturing technique assuming an unsteady, incompressible, laminar flow, as described by Gutiérrez-Montes et al [14, 15]. A detailed description of the governing equations and numerical techniques can be found in Berberović et al [3], Gutiérrez-Montes et al [14], Rusche [29], among others, and the reader is referred to them for further information.

The computational domain includes the whole 150 mm long injection nozzle, as well as a 100 mm long region of the discharging atmosphere. No slip conditions were imposed at the walls, atmospheric pressure at the air boundaries and the flow velocity at the inlets. In the case at hand, to simulate the forcing process in accordance with the experimental

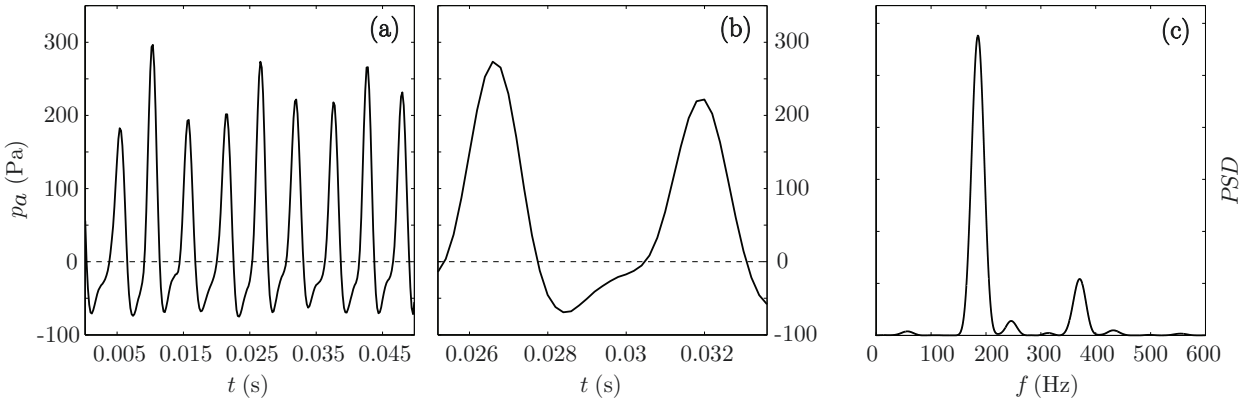

FIG. 4. The natural bubbling regime for $u_n = 2.1$ m/s ($We = 26.6$) and $u_a = 17.4$ m/s ($\Lambda = 0.118$), resulting in a bubble formation frequency of $f_n = 185$ Hz. (a) Experimental air gauge pressure, (b) detail of the air gauge pressure during a bubbling event, showing a period of negative pressure after the formation of a bubble, and (c) Power spectral density of the air gauge pressure signal exhibiting a peak at the natural bubble formation frequency, f_n.

conditions, the sinusoidal water velocity given by Eq. (6) was set as velocity inlet upstream of the nozzle exit, as illustrated in Fig. 2(d). Finally, to validate the procedure described by Eqs. (2)-(6) to determine the experimental water velocity signal from the water pressure measurements, the numerical pressure signal, which can be also fitted to Eq. (2) (Fig. 2c), was used in Eq. (5) to calculate the water velocity. As can be seen in Fig. 2(d), a very good agreement was achieved between the time evolution of the velocity obtained from the pressure signal and the one provided by the simulations, validating the experimental procedure followed to obtain the water velocity signal.

III. EXPERIMENTAL CHARACTERIZATION OF THE FORCING PROCESS

In the present section, the experimental results on the forced planar bubbling regime are described. The performance of the forcing process is first discussed and characterized, followed by a detailed description of the main physical mechanisms involved.

A. Performance of the forcing process

To explore the conditions under which the bubbling regime is controlled by the imposed disturbance, the capability of the forcing system was assessed by analyzing both the high-speed movies of the bubbling process (Fig. 3) and the time evolution of the air pressure at the injector outlet (Fig. 4). In the unforced case, illustrated in Fig. 3(a), the natural bubbling frequency, f_n, was obtained from images recorded with a high-speed camera, by processing the temporal evolution of the normalized mean grey level (NGL) along a spanwise line placed at a given downwards position, as described by Gutiérrez-Montes et al [15]. Indeed, when the process was periodic, the time series of the normalized mean grey level of a spanwise monitoring line exhibited an associated power spectral density (PSD) with a clear peak at f_n.

However, in the forced cases, due to optical uncertainties, the measurements of the air pressure, complemented by the high-speed recordings, were used to obtain the bubbling frequencies. Note that the air pressure registered in the natural bubbling regime (Fig. 4a) closely follows the one obtained numerically by Gutiérrez-Montes et al [14], including a stage of negative values (Figs. 4a,b). The experimental pressure signals were thus used herein to determine the bubble formation frequencies, provided that they show a characteristic peak in their associated PSD, as shown in Fig. 4(c).

The forcing of the natural bubbling regime was firstly explored and classified as *effective*, if the bubbles were formed at the forcing frequency, or *ineffective*, if they did not. On the one hand, for large enough values of the disturbance amplitude, ϵ, the effective forcing regime takes place, characterized by periodic bubbling events at the forcing frequency, f_f, featuring the release of a periodic train of monodisperse bubbles from the injector outlet, as shown in Figs. 3(b)-(e) for increasing forcing frequencies, and in Fig. 5(a) for one particular case. As can be observed in Fig. 5(b), under effective forcing conditions the air pressure signal is purely periodic and shows constant amplitude events, with a power spectral density exhibiting a single peak at the forcing frequency f_f (Fig. 5c). Note that, in addition to the bubble formation frequency, the bubble volume, V_b, also varies since $V_b = Q_a/f_f$. On the other hand, if ϵ is smaller than a critical value, ϵ_c, the forcing is not effective and cannot control the bubble formation process. In this case, an irregular generation of non-uniform bubbles is observed, the air pressure does not follow the characteristic time evolution associated with the

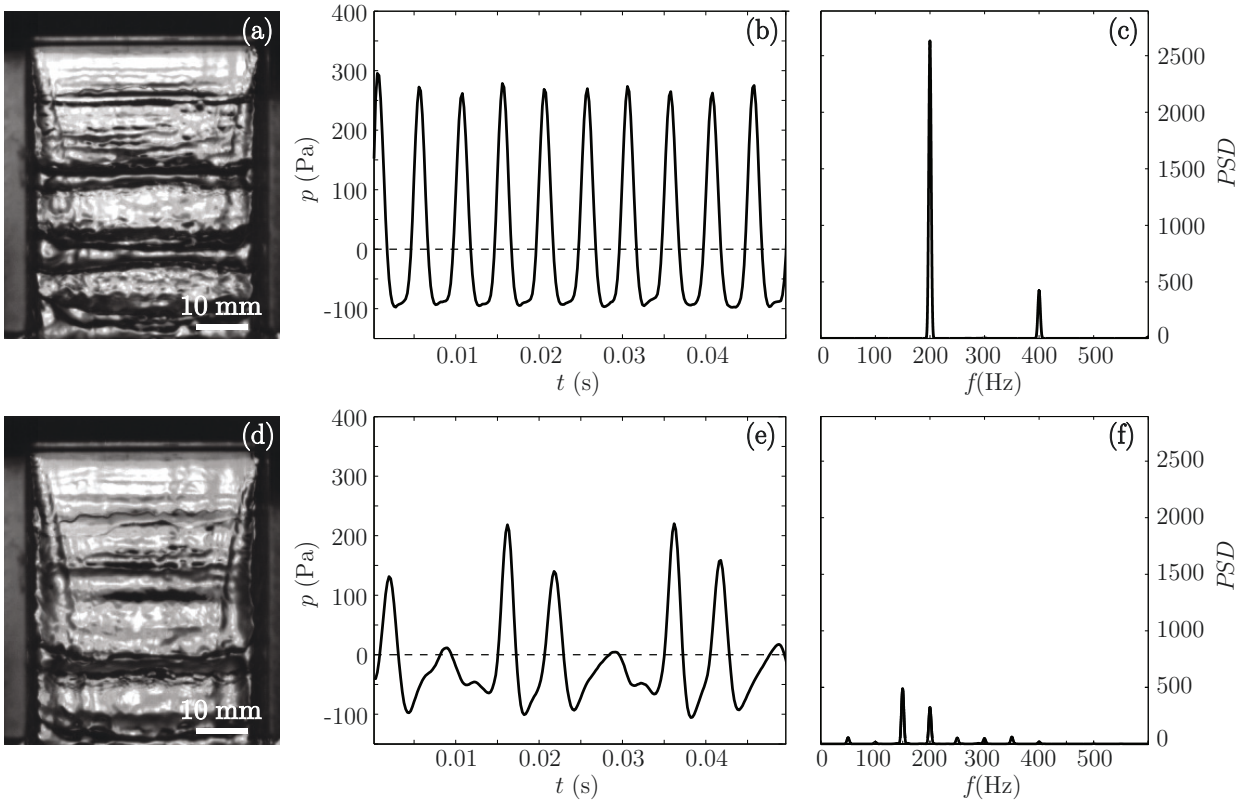

FIG. 5. Experimental results for the forced bubbling regime at $f_f = 200$ Hz for $u_n = 1.8$ m/s ($We = 21.6$) and $u_a = 14.8$ m/s ($\Lambda = 0.125$) with $f_n = 131$ Hz. First row: effective forcing process with $\epsilon = \epsilon_c = 0.039$. Second row: ineffective forcing process for $\epsilon = 0.020 < \epsilon_c$. (a), (d) Experimental images. (b), (e) Gauge pressure in the air stream. (c), (f) Power spectral density of the pressure signal.

periodic bubbling regime (Fig. 5e) and the corresponding power spectral density does not show clear peaks neither at f_f nor at f_n (Fig. 5f).

Therefore, for each pair of values (u_n,u_a), that determines a particular bubbling regime with an associated natural bubbling frequency, f_n, the *critical forcing amplitude*, ε_c, required to achieve the bubble formation at a given forcing frequency, $f_f > f_n$, i.e. an effective forcing regime, was experimentally determined. Specifically, the value of ε_c was obtained as the minimum amplitude of the water velocity modulation needed to reach an effective forcing process. In dimensionless terms, the controlled bubble formation process, defined by the values of St and Λ, is reached for dimensionless amplitudes at least equal to the critical value $\epsilon_c = \varepsilon_c/u_n$. In fact, for $\varepsilon > \varepsilon_c$ the forcing remains effective and the bubble volume is given by $V_b = Q_a/f_f$. Thus, it can be said that the critical amplitude represents a minimum and energetically optimal value.

B. Results of the effective forcing regime

In the present section, the experimental results for the critical amplitude and the length of the intact ligament, l_i, under the effective forcing regime are presented for different values of u_n, u_a, and $f_f > f_n$.

Figures 3(b)-(e) show a sequence of effective forcing regimes for increasing values of f_f, and their corresponding critical amplitudes, ε_c, which increase with f_f. It is clear that smaller bubbles are generated for increasing values of f_f, since $V_b = Q_a/f_f$ and Q_a is fixed. In addition, bubble detachment occurs closer to the nozzle as f_f increases, corresponding to smaller values of l_i. This type of analysis was extended to cover a wide range of values of u_n and u_a, determining ε_c for different values of f_f. Figure 6 summarizes the experimental results. In general terms, given the globally unstable nature of the bubbling regime [4], the flow is insensitive to small perturbations and large disturbances are required for the forcing to prevail. Indeed, it has been found that $\epsilon_c \gtrsim 0.02$ under all the conditions herein explored. These relatively large values of ϵ_c indicate the importance of nonlinear effects in the forcing phenomenon [25], as discussed in Section IV. Moreover, Fig. 6 clearly shows that, for each pair of u_n and u_a, the value of ε_c increases with f_f, as a consequence

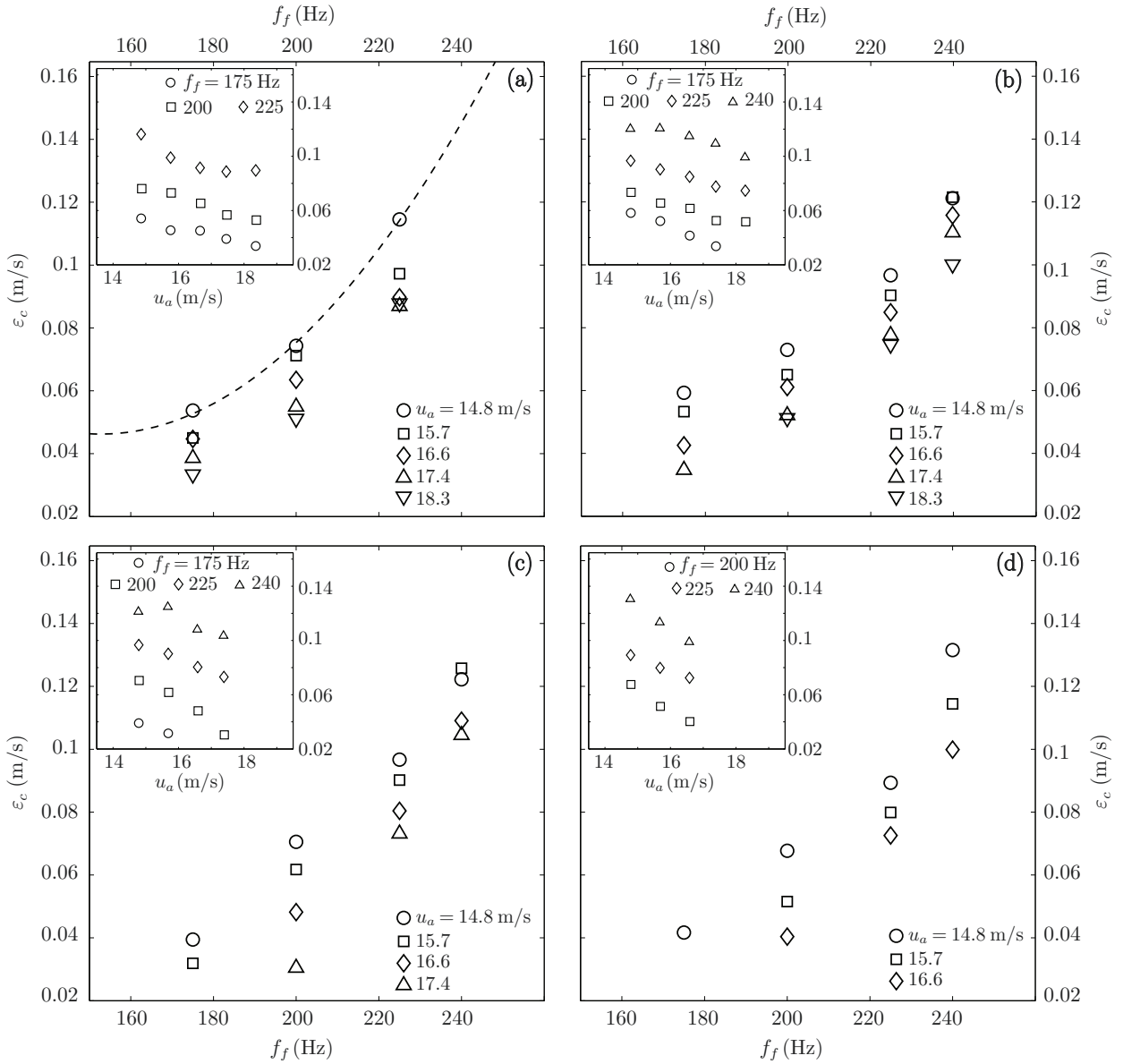

FIG. 6. Evolution of the critical amplitude of the perturbations, ε_c, as a function of f_f for several values of u_a and (a) $u_n = 1.6$ m/s, (b) $u_n = 1.8$ m/s, (c) $u_n = 2.1$ m/s, (d) $u_n = 2.3$ m/s. In the panels, each data series corresponds to a given value of u_a. The insets show ε_c versus u_a for each value of u_n. The dashed line in (a) is a fit of the form $\varepsilon_c \propto f_f^2$, indicating the quadratic dependence. Although only one data series has been fitted for clarity, all of them follow the same trend.

of the faster growth rate of the disturbance caused by the decrease of the bubble formation time, closely following a quadratic dependence $\varepsilon_c \propto f_f^2$, as revealed by Fig. 6(a). In the unforced case, the bubbling frequency is determined by the negative pressure established at the exit slit [14] and, thus, the forcing acts as an additional mechanism that allows to increase the bubble formation rate. Since the time during which the mechanism acting in the unforced case is reduced when the forcing frequency is increased, a larger forcing amplitude is required to achieve an effective forcing regime. As shown in the next Section, the forced bubbling process can be understood as a kinematic effect that modifies the natural bubbling regime.

In addition, Figure 6 also reveals that, for a fixed values of u_n and f_f, the critical amplitude decreases as the air velocity increases, a result that can be clearly observed in the insets included in each panel. This behavior is also related to the negative pressure induced by the expansion of the air stream when it discharges from the air injector into the forming bubble, $\Delta p = -\rho_a u_a^2 \beta(1-\beta)$, with $\beta = H_i/H_o$ the dimensionless thickness of the air injector. Since this effect becomes more important for increasing air velocities, a smaller forcing amplitude is required to impose a given effective forcing frequency when the air velocity grows. Nevertheless, the latter effect is likely to become weaker for values of $f_f \gg f_n$ outside the range explored herein.

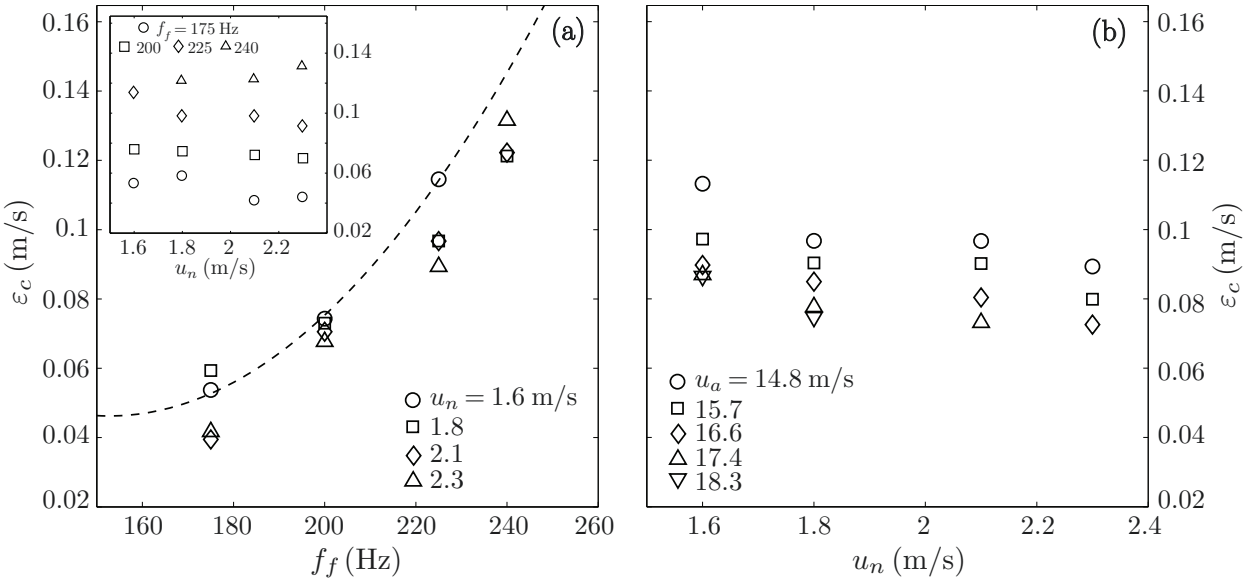

FIG. 7. Critical amplitude (a) as a function of the f_f for different values of the water velocity and for a fixed air velocity, $u_a = 14.8$ m/s, and (b) as a function of the water velocity for different values of the air velocity and for a fixed forcing frequency $f_f = 225$ Hz. The dashed line in (a) is a quadratic fit, of the form $\varepsilon_c \propto f_f^2$, to the data corresponding to $u_n = 1.6$ m/s.

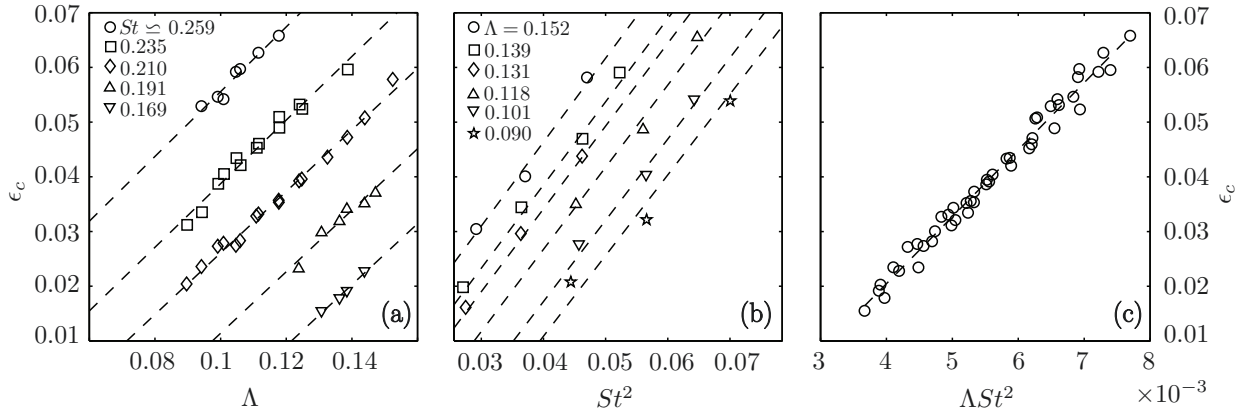

FIG. 8. Experimentally determined dimensionless critical amplitude, ϵ_c. (a) ϵ_c as a function of Λ for different values of St, and (b) ϵ_c as a function of St^2 for several values of Λ. The dashed lines in (a) and (b) are linear fits. (c) ϵ_c as a function of $\Lambda\, St^2$, showing the collapse of all the data points, with the dashed line being the linear fit given by $\epsilon_c = 12.24\,\Lambda\, St^2 - 0.028$.

To analyze the effect of u_n on ε_c, several results can be extracted from Fig. 6 and presented in Fig. 7. In particular, the value of ε_c for a fixed air velocity of $u_a = 14.8$ m/s is plotted as a function of f_f in Fig. 7(a), where the trend $\varepsilon_c \propto f_f^2$ explained before is again observed. However, unlike what happens with the air velocity, it can be observed that the value of ε_c is barely affected by u_n. Notice that, for a fixed forcing frequency, Fig. 7(b) shows a very weak effect of u_n on ε_c, compared with the effect of u_a displayed in Fig. 6 and discussed above. Therefore, it is concluded that the effect of the air velocity, u_a, on ε_c is more relevant than that of water velocity, u_n.

To have a better idea of the effects of the governing parameters, it proves convenient to represent the dependence of ε_c on f_f, u_a, and u_n, in compact form using their dimensionless counterparts. To this end, Fig. 8(a) shows that the nondimensional perturbation amplitude, ϵ_c, increases linearly with Λ for a constant value of St, consistent with the dependence of the critical forcing amplitude on the air and water velocities previously described. Moreover, Fig. 8(b) reveals that ϵ_c increases with St for a fixed value of Λ, again reflecting the dimensional result discussed above. Finally, the dependence of ϵ_c on both Λ and St can be obtained taking into account the facts that i) the critical amplitude increases quadratically with the forcing frequency, ii) decreases with the air velocity and iii) barely depends on the water velocity, i.e. $\varepsilon_c \propto f_f^2/u_a$. Indeed, Fig. 8(c) demonstrates that all the experimental data for ϵ_c collapse on a single

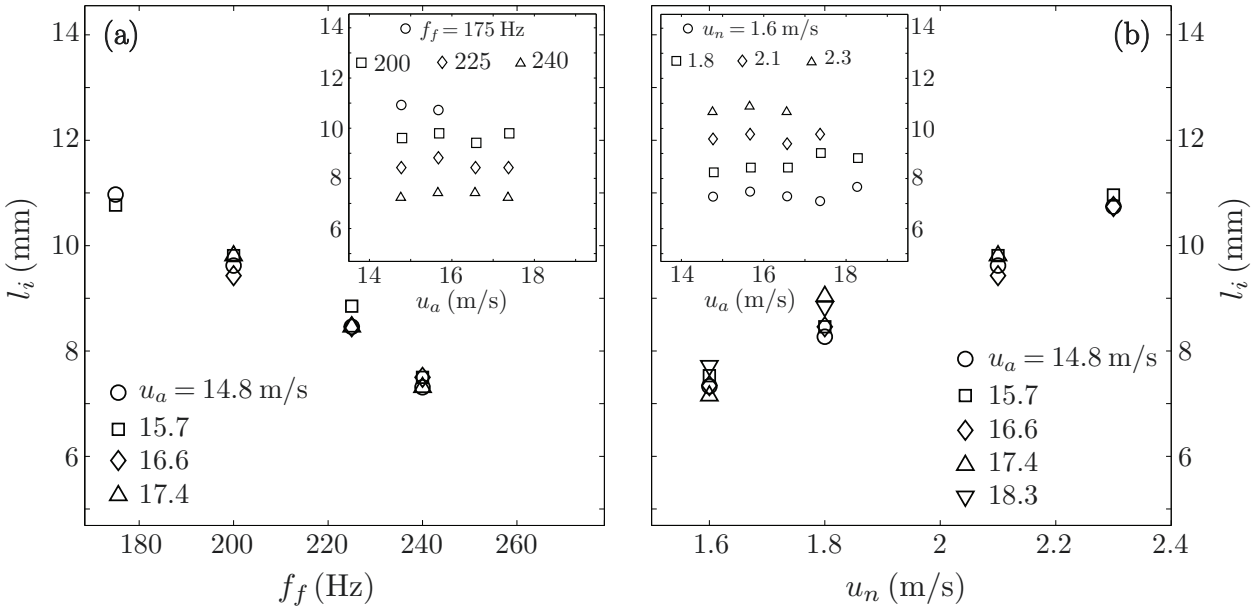

FIG. 9. Length of the intact ligament under effective forcing regime, with $\epsilon = \epsilon_c$, (a) as a function of the forcing frequency for different values of the air velocity and for $u_n = 2.1$ m/s and (b) as a function of the water velocity for different values of the air velocity and for $f_f = 200$ Hz. The insets in (a) and (b) represent the effect of the air velocity for different forcing frequencies and different water velocities, respectively.

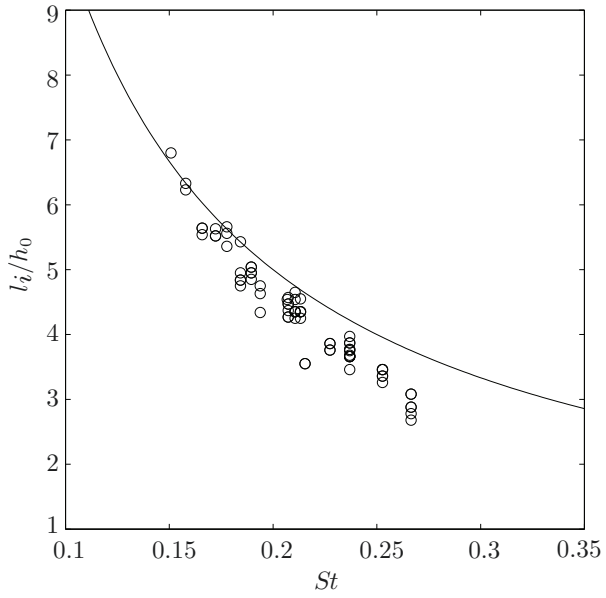

FIG. 10. Dimensionless intact length as a function of the Strouhal number for all the experiments. The solid line represents the function $l_i/h_0 = 1/St$.

curve when plotted as a function of $\Lambda\, St^2$, with the linear trend $\epsilon_c \propto \Lambda\, St^2$, indicating that $\varepsilon_c/u_n \propto u_n/u_a f_f^2 h_0^2/u_n^2$, and therefore $\varepsilon_c \propto f_f^2/u_a$.

As already commented above, the change in the bubbling frequency affects the bubble volume, $V_b = Q_a/f_f$, and modifies the length of the intact ligament, l_i, which can be estimated as $l_i = u_d/f_f$, being u_d the downstream velocity of the initial deformation that finally causes the break-up. In fact, an inspection of Fig. 9, suggests that $u_d \simeq u_n$, providing $l_i \simeq u_n/f_f$. In particular, Fig. 9(a) shows an almost linearly decrease of l_i with the forcing frequency for a given water velocity, with a negligible influence of the air velocity (see inset in Fig. 9a). Moreover, it should be noted that, for a given forcing frequency, l_i increases linearly with the water velocity, and independently of the air velocity, being the

slope nearly $1/f_f$ (see Fig. 9b). Nevertheless, for increasing forcing frequencies it has been observed that the slope becomes slightly smaller than $1/f_f$, and shorter intact lengths are obtained. This results could be associated to three dimensional instabilities triggered at higher forcing frequencies which make the bubble separate closer to the injector tip. Similar results were reported by Gutiérrez-Montes et al [14], who observed that the intact ligaments obtained from two-dimensional numerical simulations, which do not include three dimensional effects, were slightly larger than those measured experimentally (see Fig. 13 in Gutiérrez-Montes et al [14]). Furthermore, if the intact length extracted from all the experiments is plotted in dimensionless form, namely l_i/h_0, as a function of St, the data almost collapse onto a single curve that closely follows the function $1/St$, as shown in Fig. 10. Therefore, $l_i/h_0 \simeq u_n/(f_f\, h_0)$, in agreement with the conclusion that $l_i \simeq u_n/f_f$. This result has also been corroborated by the theoretical model described in Section IV, where neither three dimensional nor air stream effects have been taken into account.

IV. ANALYSIS OF THE FORCING EFFECT

In the present section, we will describe the evolution of the perturbations on the water interface based on the models provided by Meier et al [25] and Mehring and Sirignano [23], translating the origin of coordinates to $(H_o + H_w)/2$ and considering varicose perturbations. As stated in Section II A, the forcing process in the water streams produces a modulation of the water velocity at the nozzle exit (Eq. 6), complementary to the dynamic effects induced by the inner air stream, which accelerates the bubble formation mechanism. Moreover, as already pointed out in Section III, the required critical amplitudes of the imposed monochromatic perturbations for effective forcing processes are found to exceed the validity of linear analyses, mainly focused on capillary modes excited by small perturbations [9, 23, 25]. In this regard, and in order to study the direct effect of the forcing process, the water stream can be simplified and considered in first approximation as a planar sheet with free surfaces, i.e. neglecting the inner and outer aerodynamic effects, and modulated by velocity perturbations at the nozzle exit. In this case, the variations of the water velocity at the nozzle outlet generate kinematic waves in the water stream which grow downstream, inducing unsteady deformations of the liquid sheet [23, 25]. Specifically, the liquid velocity increases and decreases periodically in time, and the portions of liquid that exit the nozzle faster end up reaching the previous slower ones, resulting in the formation of a liquid cluster per cycle. Consequently, the planar sheet cross section transversely grows around the slow liquid location while it becomes thinner where the faster liquid was. These spatially growing fluid agglomerations present the convective nature of harmonic dilational waves generated at the nozzle exit, which result in bulges interspaced by almost a wavelength [23]. According to the experimental results, the break-up lengths are found to be closely equal to the perturbation wavelengths (Fig. 10), being much longer than the liquid sheet thickness. Thus, considering this long-wavelength assumption, an accurate description of the behavior of the free surfaces can be assured by a one-dimensional unsteady formulation [9, 36].

Assuming a two-dimensional incompressible, inviscid water stream in the (x, y) plane emerging from a nozzle into a gaseous atmosphere, and neglecting aerodynamic and gravitational effects, the mass conservation and momentum equations for the water sheet write,

$$\frac{\partial u_w}{\partial x} + \frac{\partial v_w}{\partial y} = 0, \tag{7}$$

$$\frac{\partial u_w}{\partial t} + u_w \frac{\partial u_w}{\partial x} + v_w \frac{\partial u_w}{\partial y} + \frac{1}{\rho_w}\frac{\partial p_w}{\partial x} = 0, \tag{8}$$

$$\frac{\partial v_w}{\partial t} + u_w \frac{\partial v_w}{\partial x} + v_w \frac{\partial v_w}{\partial y} + \frac{1}{\rho_w}\frac{\partial p_w}{\partial y} = 0, \tag{9}$$

being v_w the fluid velocity in the y-direction. Following a derivation similar to Mehring and Sirignano [23], which results in an equivalent inviscid simplification of the one-dimensional formulation for cylindrical viscous jets by Eggers and Dupont [8], the system (7)-(9) can be reduced to a one-dimensional approximation. A normal stress balance at the interfaces eliminates the pressure from the formulation keeping the surface tension effects [19]. This leads to a more realistic representation than the analytic solution proposed by Meier et al [25], where the surface tension is neglected and the sheet local thickness blows up to infinity, specially for large Strouhal numbers.

If the local liquid sheet thickness and its centerline position are denoted by $h = h(x, t)$ and $y_c = y_c(x, t)$, respectively, the dependent variables (u_w, v_w, p_w) can be expressed by a power-series expansion in terms of $(y - y_c)$ [23]. Taking h_0 and u_n as the reference magnitudes, we introduce the dimensionless quantities, $\hat{u} = u_w/u_n$, $\hat{h} = h/h_0$, $x^* = x/h_0$

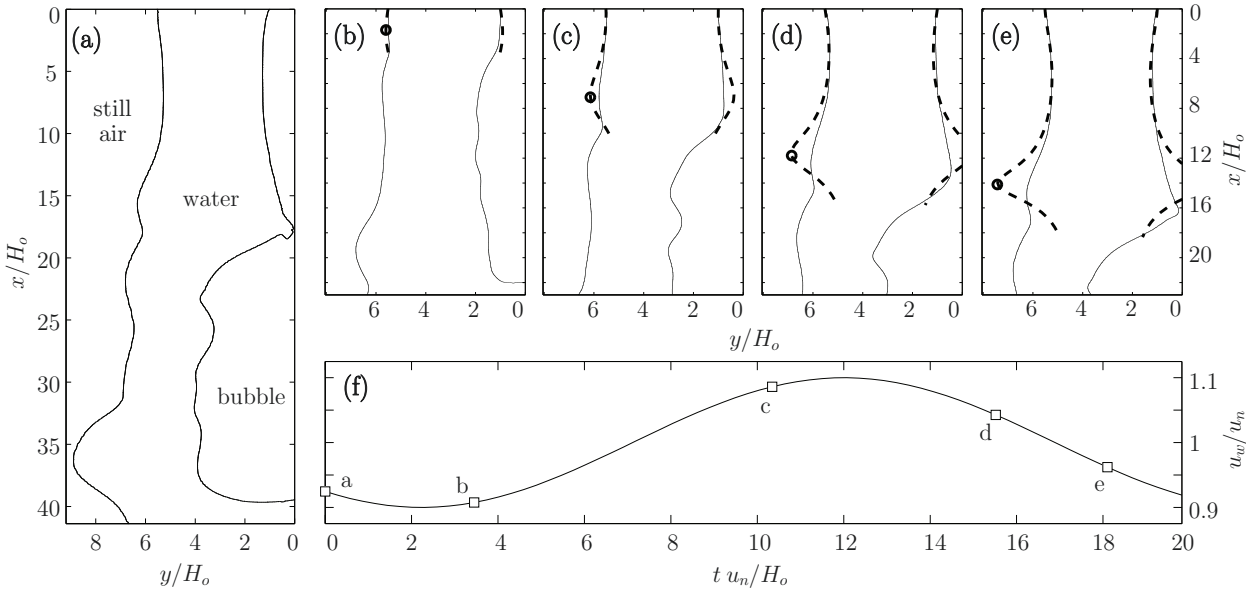

FIG. 11. (a)-(e) Inner and outer water interfaces at different instants during a forced bubble formation cycle corresponding to $We = 38.8$ and $\Lambda = 0.147$, with $f_f = 294$ Hz, where the solid lines represent the results given by numerical simulations and the dashed lines are the prediction of the one-dimensional model (Eqs. 10-11) with $We_w = 176.1$ and $\epsilon = 0.1 > \epsilon_c = 0.065$. (f) Time evolution of the numerical modulated water velocity at the nozzle exit during the whole event, where the instants showed in (a)-(e) are indicated.

and $t^* = t/(h_0/u_n)$. In addition, considering that the velocity modulation just induces dilational perturbations on the liquid sheet, only variations of $\hat{h}$ and $\hat{u}$ appear [17, 23, 25]. Therefore, the system (7)-(9) is reduced to the dimensionless leading order one-dimensional equations,

$$\frac{\partial \hat{h}}{\partial t^*} = -\frac{\partial}{\partial x^*}(\hat{u}\hat{h}), \tag{10}$$

$$\frac{\partial \hat{u}}{\partial t^*} = \frac{\partial}{\partial x^*}\left\{\frac{1}{2We_w}\left[1+\frac{1}{4}\left(\frac{\partial \hat{h}}{\partial x^*}\right)^2\right]^{-3/2}\frac{\partial^2 \hat{h}}{\partial x^{*2}} - \frac{\hat{u}^2}{2}\right\}, \tag{11}$$

where $We_w = \rho_w u_n^2 h_0/\sigma$ represents the Weber number evaluated using the characteristic magnitudes of the unforced water sheet. Equations (10) and (11) define a closed hyperbolic system in the conservative form for $\hat{h}$ and $\hat{u}$. The initial conditions are given by the steady solutions, i.e. the unforced case, and the boundary conditions at the nozzle outlet ($x^* = 0$) are

$$\hat{h}(0, t^*) = 1, \tag{12}$$

$$\hat{u}(0, t^*) = u_{w,0}(t)/u_n, \tag{13}$$

where $u_{w,0}(t)$ is the modulated velocity given by Eq. (6). The system has been solved as an initial and boundary value problem by means of an explicit finite-difference scheme, using the Richtmyer splitting of the Lax-Wendroff method. Equations (10) and (11) are discretized on a uniform staggered grid, where the spatial derivatives of $\hat{h}$ in Eq. (11) are firstly obtained by the second-order central-difference scheme for first derivatives and the first-order one for second derivatives. The time integration involves a two-step scheme with a first-order Lax predictor and a second-order leapfrog corrector [16]. The accuracy of the numerical scheme has been checked by successive refinement of the mesh size and time step. A number of grid points per wavelength of 125 and a dimensionless time step of 0.001 was found to be appropriate for a grid-independent solution.

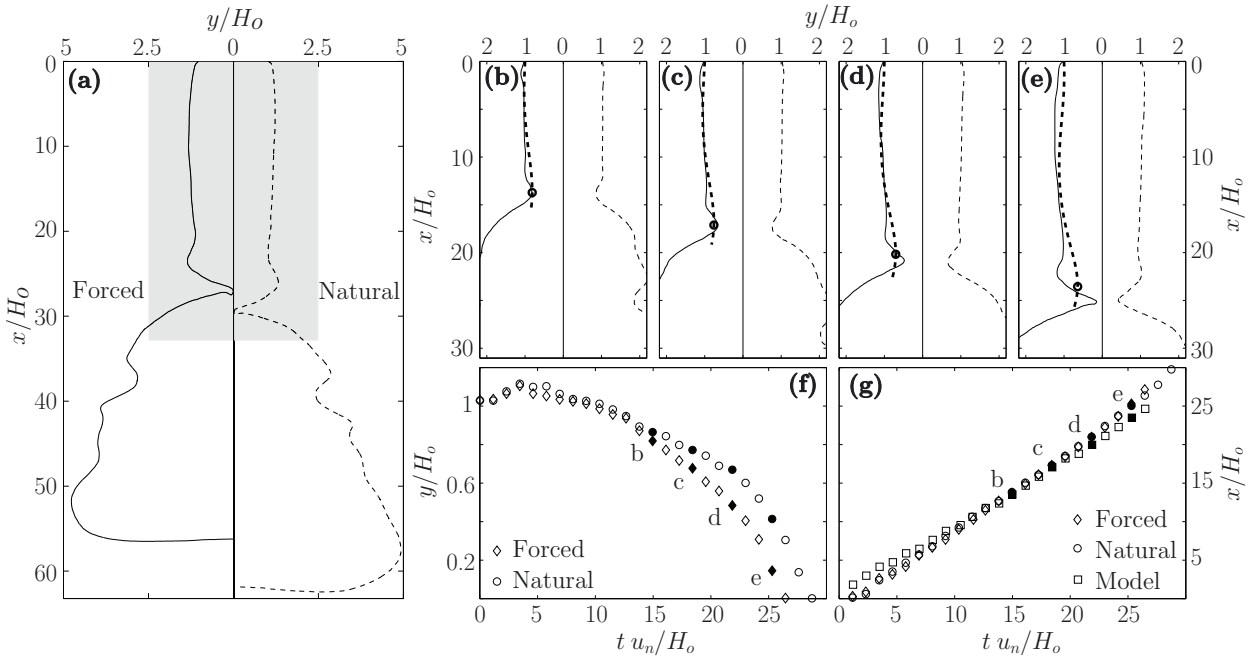

FIG. 12. Comparison of a natural bubbling process, corresponding to $We = 38.8$ and $\Lambda = 0.147$, $f_n = 196$ Hz, with the effectively forced one at $f_f = 216$ Hz and $\epsilon = 0.025 \simeq \epsilon_c = 0.022$. (a) Inner interface obtained by means of numerical simulations for the forced case (left side, solid line) and for the unforced process (right side, dashed line) at the pinch-off moment. (b)-(e) Same as (a) but in region around the narrowest section (denoted neck), and together with the inner interface calculated with the one-dimensional approach for the forced case (thick dashed line), at different instants during the bubbling cycle. A circle has been used to indicate the maximum deformation given by the model. (f) Time evolution of both the forced and natural protuberances given by the simulations along the y-direction. (g) Time evolution of the forced and natural numerical protuberances along the x-direction, together with that given by the model.

As described in Gutiérrez-Montes et al [14], the dynamic phenomena induced by the inner air stream triggers the bubble formation process in the unforced case. However, when the forcing amplitude is sufficiently large, the water sheets are mainly destabilized by the external perturbations and the one-dimensional approach defined by the system (10)-(13) can qualitatively describe the evolution of the imposed disturbances, giving a good prediction for the location of the maximum amplitude, i.e. the external cluster crest formed from the previous pinch-off event. Thus, in order to assess the prediction of Eqs. (10)-(11), since the experimental images do not show the (x, y) view, the evolution of the water interface is compared in Fig. 11 with that given by two-dimensional, unsteady, numerical simulations performed with OpenFOAM during a whole bubble formation cycle. For the sake of clarity, the value of the imposed disturbance analyzed in Fig. 11 is larger than the critical one to better appreciate its effect on the water sheet. Solutions of Eqs. (10)-(11) have been plotted from the nozzle outlet ($x = 0$) to a position slightly larger than $x_d(t^*)$, being x_d the streamwise location of the maximum deformation, at different instants over a whole cycle to clearly identify the position where the calculated cross section reaches a local maximum. Specifically, Fig. 11(a) corresponds to a pinch-off event obtained from the numerical simulations, showing the formed bubble as well as the intact ligament, which starts to inflate due to overpressure generated during the bubble collapse. At this moment, a new cycle begins, in which the liquid leaves the nozzle with low velocity (Fig. 11f), while a small bump (incipient neck) starts to form towards the air stream in the inner interface, close to the nozzle exit, due to the sudden decrease of pressure in the air sheet. As the water velocity at the exit increases (Fig. 11b), the one-dimensional model predicts a slight increment of thickness in the water sheet, which grows downstream as time evolves (Fig. 11c-e). It can be observed that the amplitude of the perturbation is larger than that obtained numerically. This might be because the model considers a free water sheet and does not take into account any effect of the air stream or coupled effects between the two water sheets. In fact, notice that, in Fig. 11(e) the amplitude of the perturbation in the inner interface is considerably larger than the outer one, corroborating that there is an influence of the fast stream of air that flows between the two water sheets in the growth rate of the perturbations. An additional effect that has not been included in the model is the influence to the forming bubble in the development of the perturbation. Thus, as the forming bubble grows, the liquid stream around it accelerates, stretching the outer air-liquid interface and, consequently, inhibiting the growth of the perturbation. Nevertheless, it can be observed in Figs. 11(b)-(e) that the downstream longitudinal position of the maximum deformation, indicated by a circle, is well predicted by the model (Eqs. 10-11), particularly in the outer interface.

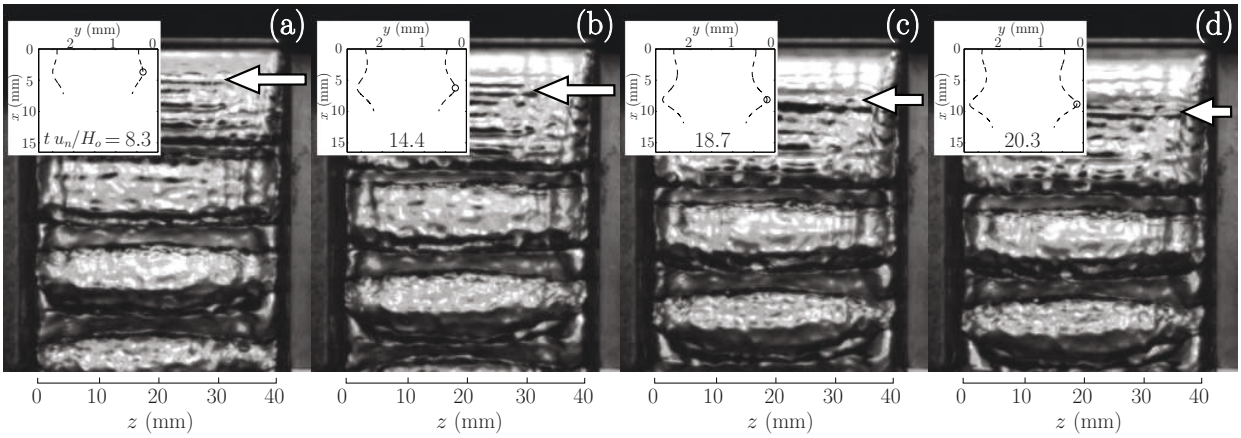

FIG. 13. Experimental images showing the spanwise view of the sheets, (x, z), of some instants during a forced bubble formation cycle corresponding to $We = 21.5$ and $\Lambda = 0.125$, with $f_n = 131$ Hz, under a forcing frequency equal to $f_f = 200$ Hz, and for $\epsilon = \epsilon_c = 0.039$. Each snapshot includes a panel in which the corresponding transverse view, (x, y), of the water stream thickness, provided by Eqs.(10)-(13), is represented with the same x-coordinate scale as in the experimental image. A circle is used to indicate the position of the maximum thickness given by the model. The horizontal arrows have been added to point the downstream position of the maximum deformation of the water interface in each panel.

Since the critical amplitude ε_c is the minimum one which properly controls the bubble formation at the desired frequency $f_f > f_n$, the maximum of the liquid bulge produced by the forcing effect must be located in the vicinity of the initial protuberance that is generated at the beginning of the cycle, i.e. the naturally induced incipient neck, adding its growth to the aforementioned dynamic effects. Moreover, it has been found that the maximum possible deformation for ε_c at each cycle and in a distance up to $u_{w,0}(t = 0)/u_n T^*$, being $T^* = u_n/(f_f h_0) = 1/St$ the period corresponding to the dimensionless forcing frequency, is reached when the forcing signal is in phase with the bubble pinch-off. In that case, the location of this local maximum results in $x_d(T^*) = u_n/f_f$, coinciding with the perturbation wavelength and in good agreement with the experimental results, as shown in Fig. 10. This facts can be explored in Fig. 12, where an effective forced case is compared with its unforced counterpart. In Fig. 12(a) it can be observed that, in accordance with the previous section, since u_n is kept constant in both cases, the increment in the bubble formation frequency leads to a reduction in the final bubble volume and, consequently, in l_i. Figs. 12(b)-(e) show a larger growth of the initial protuberance towards the symmetry plane in the forced case in comparison with the natural transverse evolution of the interface at the narrowest point. Indeed, Fig. 12(f), which shows the time evolution of the air stream semi-thickness in the narrowest section (denoted neck hereafter), indicates its closure is faster in the forced case. In addition, it can be appreciated that the longitudinal evolution of the neck location is the same in both cases (Fig. 12g), with velocities nearly equal to u_n. Nevertheless, the x-position given by the model slightly differs that obtained numerically (Fig. 12g), which indicates that the phase speed of the perturbation remains between the maximum and the minimum values of the modulated velocity [36]. Note that, despite the differences, the theoretical liquid cluster nearly coincides with the natural neck for most of the cycle (Figs. 12b-d), meanwhile the larger discrepancies occur at the cycle beginning, when the growth of the bulge is still very small, and at last instants (Fig. 12e), when the effect of the air stream during the collapse event violently accelerates the neck towards the symmetry plane.

Finally, Fig. 13 compares the theoretical prediction of the water sheet thickness as well as the local maximum deformation (indicated by a circle) with the experimental visualizations. In the (x, z) plane view showed by the images, the downstream position of the maximum deformation corresponds to a dark horizontal stripe, highlighted by a white arrow for clarity, which is more evident in Figs.13(c)-(d). It can be appreciated how the x-position of the bulge observed in the images is well predicted by Eqs. 10-11. Furthermore, the last snapshot (Fig. 13d) represents the pinch-off event, in which the air sheet appears completely broken in a position nearby the theoretical bulge crest, which corroborates the good agreement between the experiments and the one-dimensional model.

V. CONCLUSIONS

The present work reports a novel technique to control the bubbling process naturally established in a water-air-water planar co-flow configuration, with the aim of producing monodisperse bubbles of a prescribed volume at a constant rate. For such purpose, a forcing system that modulates the water flow rate has been designed and implemented. Thus, the

water sheets are forced at the nozzle exit by a monochromatic perturbation of the form $u_{w,0}(t) = u_n + \varepsilon \sin(\omega t + \varphi)$, where u_n is the unforced water velocity and ε the forcing amplitude, which is experimentally obtained from measurements of the pressure variations inside the water stream upstream from the injector exit.

The experimental results indicate that the bubbling process can be controlled to obtain a periodic formation of monodisperse bubbles of volume $V_b = Q_a/f_f$ at a desired frequency, $f_f > f_n$. The controlled bubbling process of an otherwise unforced natural, bubbling regime, characterized by the Weber number, $We = \rho_w u_n^2 H_o/\sigma$, and the water-to-air velocity ratio, $\Lambda = u_n/u_a$, can be accomplished by forcing the water stream at a given frequency, f_f, with an amplitude, ε, larger than a certain critical one, ε_c. In fact, a wide range of natural bubbling regimes have been forced at different frequencies with the aim at establishing the corresponding values of ε_c. The results obtained show a dependence of the form $\varepsilon_c \propto f_f^2$, as a consequence of the faster growth rate of the disturbance that is required when the forcing frequency increases. Moreover, a relevant influence of the air velocity on ε_c has been observed within the analyzed experimental range, which is an effect related to the underpressure induced by the air stream at the nozzle exit [14]. Therefore, for a given forcing frequency, decreasing values of ε_c are needed as the air velocity increases. In contrast with the important influence of the air velocity, a very weak dependence of ε_c on the mean water velocity, u_n, has been found. These dependencies have been confirmed when the dimensionless critical amplitude, $\epsilon_c = \varepsilon_c/u_n$, is expressed as a function of $\Lambda\, St^2$, showing that $\epsilon_c \propto \Lambda\, St^2$. In addition, the experimental measurements of the intact length, l_i, reveal a linear dependence on both the water velocity and forcing frequency and a negligible dependence on the air velocity. In particular, shorter values of l_i are found for increasing values of f_f, meanwhile increasing values of l_i have been observed for increasing water velocities. The results reported indicate that the air stream has an important influence on the transverse dynamics of the air-water interface, that is, on the growth and collapse of the neck through the induced inner underpressures and consequently on the required critical amplitudes. However, it has an almost negligible effect on the longitudinal dynamics, i.e. on the downwards traveling velocity of the deformation that finally causes the break-up. In fact, the inverse of the dimensionless break-up lengths linearly increases with the dimensionless forcing frequency, $h_0/l_i \simeq St$, resulting in $l_i \simeq u_n/f_f$.

Moreover, the effects of the forcing process over the water stream, which are complementary to the effects induced by the air stream, are found to be of purely kinematic nature. Indeed, the temporal fluctuations of the liquid velocity, induced by the imposed monochromatic perturbation, result in the formation of liquid bulges that grow transversely as they propagate downstream. Thus, a one-dimensional model has been implemented to describe the evolution of the air-water interface of the forced water sheet. It has been found that, for critical amplitudes, the position of local maximum deformation provided by the model closely follows the temporal evolution of the neck obtained both experimental and numerically, corroborating the applicability of the model. Furthermore, since the critical amplitude represents the minimum value required to reach an effective forcing process, the local maximum transverse deformation in a given cycle is achieved for a forcing signal in phase with the bubble pinch-off, resulting in a location of the bulge maximum equal to the perturbation wavelength. This result is in a good agreement with the break-up lengths obtained from the experiments.

ACKNOWLEDGMENTS

This work has been supported by the Spanish MINECO (Subdirección General de Gestión de Ayudas a la Investigación), Junta de Andalucía and European Funds, grants Nos. DPI2014-59292-C3-1-P, DPI2014-59292-C3-3-P, P11-TEP7495. Financial support from the University of Jaén, Project No. UJA2013/08/05, is also acknowledged.

[1] Abe K, Sanada T (2015) The mechanism of bubble generation using a slit elastic tube and an acoustic pressure wave in the gas phase. Chem. Eng. Sci. 128:28–35
[2] Amand L, Olsson G, Carlsson B (2013) Aeration control - a review. Water Sci. Technol. 67, 2374–2398
[3] Berberović E, van Hinsberg N, Jakirlić S, Roisman I, Tropea C (2009) Drop impact onto a liquid layer of finite thickness: Dynamics of the cavity evolution. Phys. Rev. E 79,036306
[4] Bolaños-Jiménez R, Sevilla A, Gutiérrez-Montes C, Sanmiguel-Rojas E, Martínez-Bazán C (2011) Bubbling and jetting regimes in planar coflowing air-water sheets. J. Fluid Mech. 682:519–542
[5] Bolaños-Jiménez R, Sevilla A, Martínez-Bazán C (2016) Modeling of the bubbling process in a planar co-flow configuration. Int. J. Multiphase Flow 82:86–92
[6] Chaudhary K, Maxworthy T (1980) The nonlinear capillary instability of a liquid jet. Part 2. Experiments on jet behaviour before droplet formation. J. Fluid Mech. 96(02):275–286
[7] Chuang SC, Goldschmidt VW (1970) Bubble formation due to a submerged capillary tube in quiescent and coflowing streams. Trans. ASME D: J. Basic Engng. 92:705–711

[8] Eggers J, Dupont TF (1994) Drop formation in a one-dimensional approximation of the navier–stokes equation. J. Fluid Mech. 262:205–221

[9] Eggers J, Villermaux E (2008) Physics of liquid jets. Rep. Prog. Phys. 71:036,601

[10] Gordillo JM, Gañán-Calvo AM, Pérez-Saborid M (2001) Monodisperse microbubbling: Absolute instabilities in coflowing gas-liquid jets. Phys. Fluids 13:3839–3842

[11] Gordillo JM, Cheng Z, Márquez M, Gañán-Calvo AM, Weitz DA (2004) A new device for the generation of microbubbles. Phys. Fluids 16:2828–2834

[12] Gordillo JM, Sevilla A, Martínez-Bazán C (2007) Bubbling in a coflow at high Reynolds numbers. Phys. Fluids 19:077,102

[13] Guerrero J, González H, García F (2012) Spatial modes of capillary jets, with application to surface stimulation. J. Fluid Mech. 702:354–377

[14] Gutiérrez-Montes C, Bolaños-Jiménez R, Sevilla A, Martínez-Bazán C (2013) Experimental and numerical study of the periodic bubbling regime in planar co-flowing air-water sheets. Int. J. Multiphase Flow 50:106–119

[15] Gutiérrez-Montes C, Bolaños-Jiménez R, Sevilla A, Martínez-Bazán C (2014) Bubble formation in a planar water-air-water jet: Effects of the nozzle geometry and the injection conditions. Int. J. Multiphase Flow 65:38–50

[16] Hirsch C (2007) Numerical Computation of Internal and External Flows: The Fundamentals of Computational Fluid Dynamics. Butterworth-Heinemann

[17] Kim I, Sirignano WA (2000) Three-dimensional wave distortion and disintegration of thin planar liquid sheets. J. Fluid Mech. 410:147–183

[18] Krishna R, Ellenberger J (2003) Influence of low-frequency vibrations on bubble and drop sizes formed at a single orifice. Chem. Eng. and Process 42(1):15–21

[19] Lee HC (1974) Drop formation in a liquid jet. IBM J. Res. Dev. 18(4):364–369

[20] Lozano A, García-Olivares A, Dopazo C (1998) The instability growth leading to a liquid sheet breakup. Phys. Fluids 10(9):2188–2197

[21] Makuta T, Takemura F, Hihara E, Matsumoto Y, Shoji M (2006) Generation of micro gas bubbles of uniform diameter in an ultrasonic field. J. Fluid Mech. 548:113–131

[22] Makuta T, Suzuki R, Nakao T (2013) Generation of microbubbles from hollow cylindrical ultrasonic horn. Ultrasonics 53(1):196–202

[23] Mehring C, Sirignano WA (1999) Nonlinear capillary wave distortion and disintegration of thin planar liquid sheets. J. Fluid Mech. 388:69–113

[24] Mehring C, Sirignano WA (2001) Nonlinear capillary waves on swirling, axisymmetric free liquid films. Int. J. Multiphase Flow 27:1707–1734

[25] Meier GEA, Klöpper A, Grabitz G (1992) The influence of kinematic waves on jet break down. Exp. Fluids 12(3):173–180

[26] Oğuz HN, Prosperetti A (1993) Dynamics of bubble growth and detachment from a needle. J. Fluid Mech. 257:111–145

[27] Ohl C (2001) Generator for single bubbles of controllable size. Rev. Sci. Instrum. 72(1):252–254

[28] Rodríguez-Rodríguez J, Sevilla A, Martínez-Bazán C, Gordillo JM (2015) Generation of microbubbles with applications to industry and medicine. Annu. Rev. Fluid Mech. 47:405–429

[29] Rusche H (2002) Computational fluid dynamics of dispersed two-phase flows at high phase fractions. PhD thesis, Imperial College of Science, Technology and Medicine, London

[30] Sevilla A, Gordillo JM, Martínez-Bazán C (2002) The effect of the diameter ratio on the absolute and convective instability of free coflowing jets. Phys. Fluids 14:3028–3038

[31] Sevilla A, Gordillo JM, Martínez-Bazán C (2005) Bubble formation in a coflowing air-water stream. J. Fluid Mech. 530:181–195

[32] Shirota M, Sanada T, Sato A, Watanabe M (2008) Formation of a submillimeter bubble from an orifice using pulsed acoustic pressure waves in gas phase. Phys. Fluids 20(4):043,301

[33] Sirignano WA, Mehring C (2000) Review of theory of distortion and disintegration of liquid streams. Prog. Energy Comb. Sci. 26(4-6):609–655

[34] Stone HA, Strook AD, Adjari A (2004) Engineering flows in small devices: Microfluidics toward a lab-on-a-chip. Annu. Rev. Fluid Mech. 36:381–411

[35] Vejrazka J, Fujasová M, Stanovsky P, Ruzicka MC, Drahoš J (2008) Bubbling controlled by needle movement. Fluid Dyn. Res. 40(7):521–533

[36] Zhu Y, Oğuz HN, Prosperetti A (2000) On the mechanism of air entrainment by liquid jets at a free surface. J. Fluid Mech. 404:151–177